



Wavelet-based defect detection in solar wafer images with inhomogeneous texture

Wei-Chen Li, Du-Ming Tsai*

Department of Industrial Engineering and Management, Yuan-Ze University, 135 Yuan-Tung Road, Nei-Li, Tao-Yuan, Taiwan, ROC

ARTICLE INFO

Article history:

Received 24 June 2011

Accepted 28 July 2011

Available online 3 August 2011

Keywords:

Surface inspection

Defect detection

inhomogeneous texture

Solar wafer

Wavelet transform

ABSTRACT

Solar power is an attractive alternative source of electricity. Multicrystalline solar cells dominate the market share owing to their lower manufacturing costs. The surface quality of a solar wafer determines the conversion efficiency of the solar cell. A multicrystalline solar wafer surface contains numerous crystal grains of random shapes and sizes in random positions and directions with different illumination reflections, therefore resulting in an inhomogeneous texture in the sensed image. This texture makes the defect detection task extremely difficult. This paper proposes a wavelet-based discriminant measure for defect inspection in multicrystalline solar wafer images.

The traditional wavelet transform techniques for texture analysis and surface inspection rely mainly on the discriminant features extracted in individual decomposition levels. However, these techniques cannot be directly applied to solar wafers with inhomogeneous grain patterns. The defects found in a solar wafer surface generally involve scattering and blurred edges with respect to clear and sharp edges of crystal grains in the background. The proposed method uses the wavelet coefficients in individual decomposition levels as features and the difference of the coefficient values between two consecutive resolution levels as the weights to distinguish local defects from the crystal grain background, and generates a better discriminant measure for identifying various defects in the multicrystalline solar wafers. Experimental results have shown the proposed method performs effectively for detecting fingerprint, contaminant, and saw-mark defects in solar wafer surfaces.

Crown Copyright © 2011 Published by Elsevier Ltd. All rights reserved.

1. Introduction

Image analysis techniques are widely used for visual surface inspection in automated manufacturing to ensure product quality and yield. The machine vision algorithms designed for surface defect detection are usually implemented on non-textured surfaces such as paper and glass materials, or on homogeneously-textured surfaces such as textile fabrics and sandpapers, or on repeated patterns such as semiconductor wafer dies and liquid crystal display (LCD) panels. Those algorithms are able to distinguish local anomalies that break the consistency or homogeneity of their surrounding background. The surface defect detection task generally involves non-quantifiable, ill-defined faulty items such as cracks, wears and contaminants. This research develops an automatic visual inspection algorithm for non-quantifiable defects in a multicrystalline solar wafer surface that contains inhomogeneous patterns in the image.

Recent advances in surface defect detection [1] show that most of the machine vision techniques are based on texture analysis. For uniform/non-textured surface images, the requirement of defect detection has arisen in glass plates [2,3], sheet steel [4], aluminum strips [5], and web materials [6]. Defects in these uniform images can be effectively identified with simple statistical measures such as the mean and variance of gray levels. They can also be easily detected using simple thresholding or edge-detection techniques. For repeated pattern images, automated visual inspection has been successfully applied to a wide variety of material surfaces found in industry, such as semiconductor wafers [7–9], textile fabrics [10,11], and screen-printed solar cells [12,13]. The detection techniques for these images generally use comparison methods such as template matching or self-generating template.

For homogeneously-textured surfaces, the texture pattern enclosed in a small neighborhood window shows high similarity everywhere in the image, such as polishing [14] or casting surfaces [15]. The defect detection methods for textured surfaces can generally be categorized into two types, spatial and spectral approaches. In the spatial domain, the commonly used texture features are the second-order statistics derived from spatial gray-level co-occurrence matrices [16]. They have been applied to wood inspection [17], carpet wear assessment [18], roughness measurement of machined

* Corresponding author. Fax: +886 3 4638907.

E-mail addresses: iedmtsai@saturn.yzu.edu.tw, s929501@mail.yzu.edu.tw, s968902@mail.yzu.edu.tw (D.-M. Tsai).

surfaces [19], and textile defect detection [20]. In the spectral domain, texture features are popularly derived from the power spectra using Fourier transforms [21,22]. They have been successfully applied to fabric defect detection [23,24] and semiconductor wafer inspection [25].

In the recent past, multiresolution decomposition schemes based on wavelet transforms have been a popular alternative for texture feature extraction [26,27]. The multiresolution wavelet representation allows an image to be decomposed into a hierarchy of local subimages at different spatial frequencies [28]. It divides the two-dimensional (2-D) frequency spectrum of an image into 2-D wavelet coefficient matrices. The 2-D wavelet coefficient matrices are composed of a low-pass (smooth) subimage and a set of high-pass (detail) subimages. The high-pass subimages are further divided into horizontal, vertical, and diagonal subimages. The square of a wavelet coefficient in a decomposed subimage is denoted by “wavelet energy” [29] and is typically used to describe the texture feature.

Defect detection techniques have been extensively developed for industrial inspection via feature extraction in wavelet-domain images. Wavelet decomposition has been applied to defect inspection of wafer dies [29], fabrics [30–32], light-emitting diode (LED) chips [33], tiles [34], pipe failures [35], and strongly reflected metal surfaces [36]. All these methods extract wavelet coefficients of smooth or detail subimages at individual decomposition levels as local texture features and then attempt to classify defects by independent component analysis [32], principal component analysis [33], neural networks [34], and support vector machine [36].

The above studies is considered only about the extraction of wavelet coefficients/energy from the decomposed subimages in individual resolution levels and applied only to surfaces with homogeneous textures. These representative features are always given by high frequency coefficients that correspond to a significant gray-level variation in the original image. The significant gray-level transition, such as the borders of textile texture, wood grain, and crystal boundaries, shows accordingly larger coefficients in the wavelet decomposed images.

In this study, the multicrystalline solar wafer surface shows numerous crystal grains of random shapes and sizes in random positions and directions with different illumination reflection.

These crystal grains result in an inhomogeneous pattern in the sensed image. The adjacent crystal grains in the multicrystalline solar wafer surface present significant gray-level difference and result in sharp grain boundaries. Fig. 1(a) and (b) shows two defect-free solar wafer images. The inhomogeneously textured surfaces show various and random local patterns in the background, and no two multicrystalline solar wafer images have the same crystal grain patterns. The aforementioned inspection techniques for uniform surfaces, homogeneous textures, and repetitive patterns fail to tackle the problem.

For inhomogeneously-textured surfaces, similar patterns will not repeatedly appear in the image. To detect defects in an inhomogeneous texture such as marble or granite, Ar and Akgul [37] employed eight Gabor filters to construct a feature extraction system for marble tile inspection. In their method, the average of the eight Gabor response values is calculated and three quantitative scores are used to assign the percentages of veins, spots, and swirls as the features for classification. Xie and Mirmehdi [38–40] presented an automatic defect detection method for random color-texture surfaces. It generates a set of texture exemplars by exploring a Gaussian mixture model from defect-free image patches, and uses the exemplars for defect detection in marble tiles. Liu and Pok [41] proposed a texture edge detection method that includes encoding and prediction modules for texture classification. The encoding module first projects multi-dimensional texture features onto an one-dimensional feature map through an SOFM (Self-Organizing Feature Map) algorithm to obtain scalar features, and then the prediction module computes the direction of scalar features with respect to their eight direction neighbors. They applied the method to detect defects on micro-texture images such as fabric and sand. The above-mentioned methods focus only on marbles or granites in which the surfaces do not show sharp and clear edges between grains, and present roughly homogeneous textures in their coarse resolution.

Solar power has become an attractive alternative source of electricity energy due to growing environmental concerns and the global oil shortage. Solar cells that convert the photons from the sun to electricity are mainly based on crystalline silicon in the current market because of the material's cost-effective performance on usable lifespan and conversion efficiency. Multicrystalline, instead

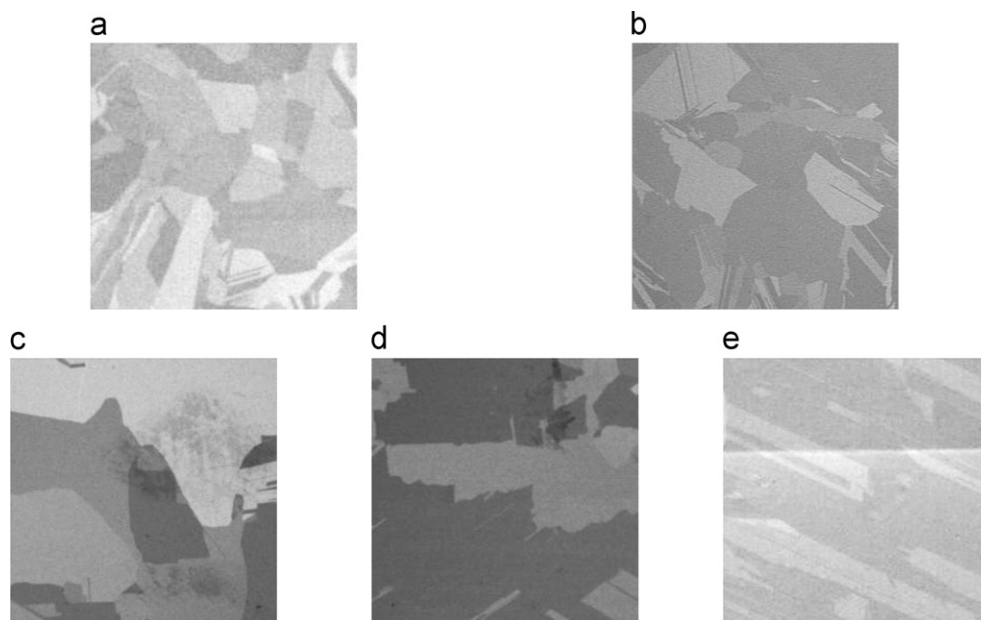


Fig. 1. Multicrystalline solar wafer images: (a), (b) two defect-free solar wafer images; (c)–(e) three types of defects in multicrystalline solar wafer surfaces: fingerprint, contaminant, and saw-mark, respectively.

of monocrystalline, materials dominate the production volume of silicon cells owing to lower material and manufacturing costs. Fig. 1(c)–(e) shows three important defect types in multicrystalline solar wafer surfaces. Fig. 1(c) contains a blurred fingerprint scattering on the crystal grain surface. Fig. 1(d) is a light contaminant at the top of the solar wafer image. Fig. 1(e) shows a saw-mark defect, which occurs from slicing the silicon ingot with a wear saw or through the impurity of silicon material. The defects on a multicrystalline solar wafer surface present relatively unclear and blurred edges, and are superimposed within a crystal grain or across sharp edges of crystal grains. The multi-grain solar wafer background makes the automatic defect detection task extremely difficult.

The defects on a solar wafer or a solar cell result in high recovery costs in the manufacturing process and reduce production yield. This calls for automatic visual inspection of solar wafers/cells. Fu et al. [42] implemented a machine vision scheme to detect edge cracks in solar cells. Their method inspected only the cracks in the solar cell edges with obvious gray-level variances. Ordaz and Lush [43] analyzed the conversion efficiency of a solar cell based on the gray-level distribution in the electroluminescence image. Pilla et al. [44] applied thermographic inspection of photovoltaic solar cells to identify cracks. Most of the solar cell inspection methods focus on efficiency assessment and edge crack detection, and the surface defects are rarely mentioned. Recently, Tsai et al. [45] proposed an anisotropic diffusion scheme for detecting micro-crack defects in multicrystalline solar wafers. The micro-crack in the sensed image presents a low gray-level and a high gradient. The diffusion model thus takes both gray-level and gradient as features to adjust the degrees of smoothness in the solar wafer image. It smoothes the suspected defect region and preserves the original gray-levels of the faultless background so that micro-cracks can be well detected by subtracting the diffused image from the original image. The anisotropic diffusion scheme works successfully for detecting micro-cracks in multicrystalline solar wafers. However, it cannot be extended to inspect all types of defects, such as the saw-marks, fingerprints, and contaminants found in multicrystalline solar wafers, because these defect types do not all present the same properties of micro-cracks.

In this study, a wavelet-based algorithm is proposed for defect detection in multicrystalline solar wafer surfaces. The traditional wavelet-based texture analysis/defect detection techniques emphasize only the combination of smooth and detail wavelet decompositions of an image, and extract the discriminant features in individual decomposition levels. But they cannot be directly applied to multicrystalline solar wafers, wherein the subtle defects and the normal crystal grain edges may present similar properties in the same wavelet decomposition level.

The defects found in a solar wafer surface generally involve scattering and blurred edges, compared to clear and sharp edges of the crystal grains in the background. In the wavelet domain, the mean wavelet energy of a decomposed subimage is gradually increased as the multiresolution level is increased. The energy increase rate of sharp grain edges is lower than that of blurred defect edges between two consecutive decomposition levels. The sharp grain edges and the relatively blurred defect edges in one decomposition level of the wavelet-domain space generally do not show distinct differences and cannot be solely used as features for discrimination. In order to extract a better measure for distinguishing defect edges from crystal grain edges, the energy differences of wavelet detail subimages in two consecutive decomposition levels are used as the weight to enhance the discriminant features extracted in individual decomposition levels, and generate a better discriminant measure for identifying various defects in multicrystalline solar wafers. A simple adaptive threshold given by a constant multiplication of the standard

deviation from the mean of all measured values in an inspection image can then be easily used to identify the defect point if the discriminant value violates the threshold.

This paper is organized as follows: Section 2 discusses the design of discriminant features of multicrystalline solar wafers in wavelet-decomposed images, followed by the detection procedure for local defects in the inhomogeneous background. Section 3 analyzes the effects of changes in parameter settings of the proposed method and presents the experimental results on various defect types. This paper is concluded in Section 4.

2. Defect detection scheme

This section presents the proposed defects detection scheme for multicrystalline solar wafer images. Section 2.1 first describes the wavelet-based feature extraction and defect identification procedure in the gray-level image of a solar wafer surface. Section 2.2 further discusses the same defect detection procedure in the gradient image and shows the benefit of feature extraction from the gradient image of a solar wafer surface.

2.1. Feature extraction from wavelet decompositions

The wavelet transform, a powerful tool for localized frequency analysis, decomposes an input signal into smooth and detailed parts with low- and high-pass filters on multiresolution levels. It is ideally suited for representing both spatial and frequency characteristics of a solar wafer image. The 1-D wavelet transform is defined as a decomposition of a signal $s(t)$ with a family of orthonormal bases $\psi_{j,k}(t)$ generated from a kernel function $\psi(t)$ by dilation j and translation k [46]:

$$\psi_{j,k}(t) = 2^{-j/2} \psi(2^{-j}t - k) \quad (1)$$

Since $\psi_{j,k}(t)$ forms an orthonormal set, the wavelet coefficients $a_{j,k}$ of the signal $s(t)$ can be calculated by the inner product:

$$a_{j,k} = \langle s(t), \psi_{j,k}(t) \rangle = \int s(t) \cdot \psi_{j,k}(t) dt \quad (2)$$

The 1-D wavelet transform can be easily extended to a two-dimensional one. The 2-D wavelet decomposition of an image $f(x,y)$ consists of filtering and down-sampling along the x -axis using the 1-D lowpass filter $l(i)$ and highpass filter $h(j)$ to generate the coefficient matrices $f_l(x,y)$ and $f_h(x,y)$. Filtering and downsampling along the y -axis then follow, using the same lowpass and highpass filters $l(i)$ and $h(j)$ for each column in $f_l(x,y)$ and $f_h(x,y)$, and produces four subimages $f_s(x,y)$, $f_H(x,y)$, $f_V(x,y)$ and $f_D(x,y)$ for one level of decomposition. $f_s(x,y)$ is a smooth subimage representing the coarse approximation of the image. $f_H(x,y)$, $f_V(x,y)$ and $f_D(x,y)$ are detail subimages representing horizontal, vertical and diagonal edges of the image. The smooth subimages $f_s(x,y)$ can be further decomposed to generate the next resolution level of the hierarchy. The 2-D pyramid wavelet decomposition algorithm for a digital image can be implemented as follows [30,31,47].

Given an image $f(x,y)$ of size $M \times N$,

$$f_l(x,y) = \frac{1}{L_l} \sum_i l(i) \cdot f((2x+i) \bmod M, y) \quad (3a)$$

$$f_h(x,y) = \frac{1}{L_h} \sum_j h(j) \cdot f((2x+j) \bmod M, y) \quad (3b)$$

for $x=0, 1, 2, \dots, (M/2)-1$ and $y=0, 1, 2, \dots, N-1$

$$f_s(x,y) = \frac{1}{L_l} \sum_i l(i) \cdot f_l(x, (2y+i) \bmod N) \quad (3c)$$

$$f_H(x,y) = \frac{1}{L_h} \sum_j h(j) \cdot f_h(x, (2y+i) \bmod N) \quad (3d)$$

$$f_V(x,y) = \frac{1}{L_l} \sum_i l(i) \cdot f_h(x, (2y+i) \bmod N) \quad (3e)$$

$$f_D(x,y) = \frac{1}{L_h} \sum_j h(j) \cdot f_h(x, (2y+i) \bmod N) \quad (3f)$$

where L_l and L_h are the support lengths of filters $l(i)$ and $h(j)$, respectively. In this study, the most compact Haar basis with lowpass filter $(l(0), l(1)) = (\sqrt{2}/2, \sqrt{2}/2)$ and highpass filter $(h(0), h(1)) = (\sqrt{2}/2, -\sqrt{2}/2)$ are used for fast convolution.

Fig. 2(a) shows a multicrystalline solar wafer image that contains a fingerprint defect. The solar wafer image shows multiple gains of random shapes and sizes and results in an inhomogeneously textured pattern. The fingerprint region is marked by a square frame in the image, and the dotted-square frame indicates a defect-free region that contains a few crystal grains. Fig. 2(b)–(c) demonstrate one level of four wavelet subimages of the defect (denoted by horizontal detail \hat{f}_H , vertical detail \hat{f}_V , diagonal detail \hat{f}_D and smooth \hat{f}_S) and the defect-free region (denoted by f_H, f_V, f_D and f_S), respectively.

In order to extract the representative features of a solar wafer, we calculate the normalized energy of each decomposed detail subimage within a small neighborhood window of size $w \times w$ with $w = k + 1$ at a resolution level ℓ . It is defined as the sum of all squared wavelet coefficients in the spatial window of a decomposed detail subimage at a resolution level with respect to that of the decomposed smooth subimage at the same resolution level. That is,

$$E_H^{(\ell)}(x,y) = F_H^{(\ell)}(x,y) / F_S^{(\ell)}(x,y) \quad (4a)$$

$$E_V^{(\ell)}(x,y) = F_V^{(\ell)}(x,y) / F_S^{(\ell)}(x,y) \quad (4b)$$

$$E_D^{(\ell)}(x,y) = F_D^{(\ell)}(x,y) / F_S^{(\ell)}(x,y) \quad (4c)$$

where

$$F_H^{(\ell)}(x,y) = \sum_{i=-k}^k \sum_{j=-k}^k [f_H^{(\ell)}(x+i, y+j)]^2$$

$$F_V^{(\ell)}(x,y) = \sum_{i=-k}^k \sum_{j=-k}^k [f_V^{(\ell)}(x+i, y+j)]^2$$

$$F_D^{(\ell)}(x,y) = \sum_{i=-k}^k \sum_{j=-k}^k [f_D^{(\ell)}(x+i, y+j)]^2$$

$$F_S^{(\ell)}(x,y) = \sum_{i=-k}^k \sum_{j=-k}^k [f_S^{(\ell)}(x+i, y+j)]^2$$

In Eqs. (4a)–(4c), $E_H^{(\ell)}(x,y)$, $E_V^{(\ell)}(x,y)$ and $E_D^{(\ell)}(x,y)$ are the normalized energies of decomposed horizontal, vertical, and diagonal detail subimages for pixel coordinates (x,y) at resolution level ℓ , respectively. The box-plot in Fig. 3(a) shows the normalized energy $E^{(\ell)}(x,y)$ at resolution level one for pixel points in the defective (denoted by $\hat{E}_D^{(1)}$, $\hat{E}_H^{(1)}$ and $\hat{E}_V^{(1)}$) and defect-free (denoted by $E_D^{(1)}$, $E_H^{(1)}$ and $E_V^{(1)}$) regions in Fig. 2(a). It indicates that the diagonal energy $E_D^{(1)}(x,y)$ can be a better discriminant feature than the horizontal energy $E_H^{(1)}(x,y)$ and vertical energy $E_V^{(1)}(x,y)$. Since the defect shows spread and blurred edges and the crystal grains present concentrated and sharp edges, the resulting diagonal energy of a defect edge is generally larger than that of a grain edge. However, the difference is neither large nor stable enough for only this energy feature to be used for discriminating defect regions from the crystal grain background.

Fig. 3(b) presents the normalized energy of the diagonal decomposition $E_D(x,y)$ at resolution levels one ($E_D^{(1)}(x,y)$), two ($E_D^{(2)}(x,y)$) and three ($E_D^{(3)}(x,y)$). It shows that the diagonal energy magnitude is distinctly increased for the blurred fingerprint edges as the resolution level is increased due to the scattering and blurred edges in the wavelet decomposition. Conversely, the diagonal energies of a defect-free region remain relatively very stable at different resolution levels

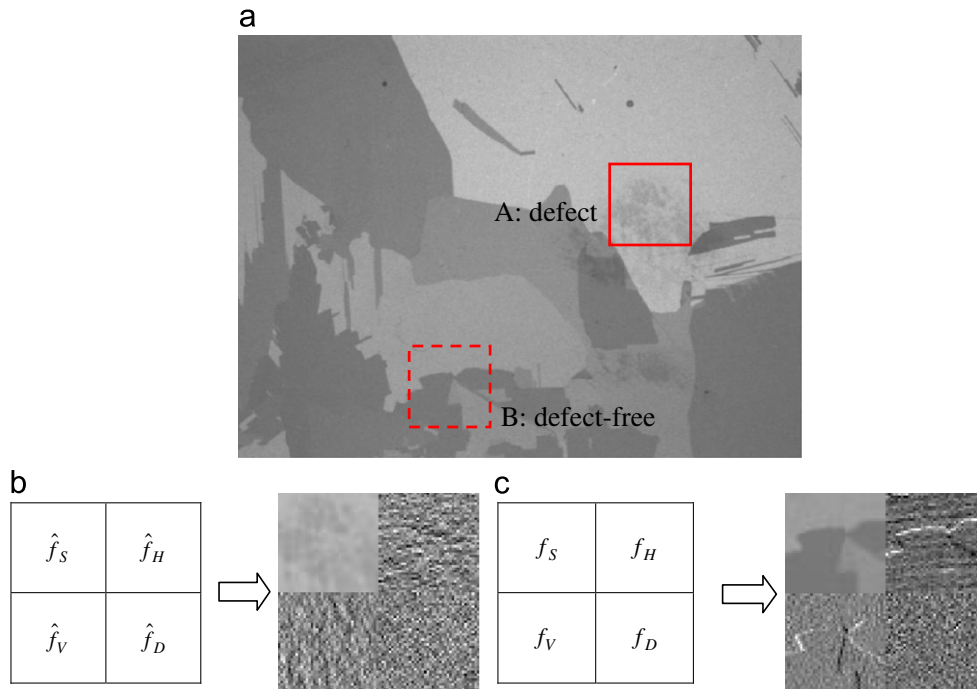


Fig. 2. (a) Fingerprint defect image; (b), (c) respective wavelet subimages of defect (frame A) and defect-free region (frame B) at decomposition level one.

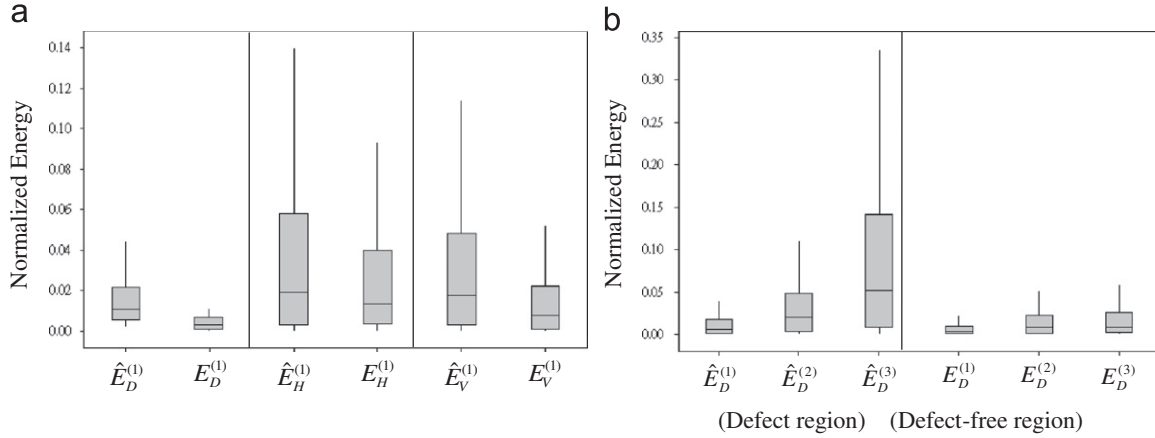


Fig. 3. Box-plots of normalized energies of detail subimages for defect and defect-free regions in Fig. 2(a): (a) Energies of various detailed subimages at resolution level one; (b) diagonal energies $E_D(x,y)$ at resolution levels one, two, and three.

due to the clear and sharp grain edges in the wavelet decomposition. The energy difference between two consecutive resolution levels can thus be further used as a weighting factor to intensify the gap of feature values between defect and defect-free regions.

In order to quantify the energy changes between two consecutive resolution levels, the average energy difference $\Delta F_{\ell,\ell+1}(x,y)$ between resolution levels ℓ and $\ell+1$ in a small neighborhood window is calculated, and it is defined as:

$$\Delta F_{\ell,\ell+1}(x,y) = \frac{1}{w^2} \tilde{F}_D^{(\ell+1)}(x,y) - \frac{1}{w^2} F_D^{(\ell)}(x,y) \quad (5)$$

where $\tilde{F}_D^{(\ell+1)}$ is resized from the diagonal energy $F_D^{(\ell+1)}$ at scale level $\ell+1$ to agree with the size of $F_D^{(\ell)}$ at scale level ℓ in order to implement the mathematical operation. Both are calculated within the neighborhood window of size $w \times w$. In this study, the window size is set to 9×9 . The average energy difference in two scale levels uses only the diagonal decomposed subimage $F_D^{(\ell)}$ because it has more discriminant power than the horizontal and vertical decomposed subimages, as mentioned before. Note that the accumulated energy of the diagonal detail is increased as the resolution level is increased, and the resulting $\Delta F_{\ell,\ell+1}$ is a positive value. A scattering and blurred defect edge generally gives a large energy difference in two scale levels, and we would like to use it to give a larger weight for the discriminant features E_D in various scale levels. A clear and sharp grain edge usually results in a smaller energy difference in two scale levels, and a smaller weight is given to the discriminant features. The additional weight information allows widening of the discriminant gap for the separation of defect edges from random crystal grain edges in the background.

The weight used to adjust the importance of the diagonal energy at a resolution level $\ell+1$ is given by

$$C_{\ell,\ell+1}(x,y) = 1 - \exp(-\Delta F_{\ell,\ell+1})$$

The weight C is in the range of 0–1. A defect edge will be assigned a larger weight for the diagonal energy $E_D^{(\ell+1)}$, and a grain edge will be given a smaller weight for the discriminant feature.

To generate a quantitative measure for detecting defects in the multicrystalline solar wafer surface, this research proposes a discriminant measure $S(x,y)$, which is combined with the normalized energies $E_D^{(\ell)}$ of decomposed diagonal subimages at three resolution levels with the $C_{\ell,\ell+1}(x,y)$ as the weights. Given an image $f(x,y)$ of size $M \times N$, the discriminant measure is calculated as follows:

$$S(x,y) = E_D^{(1)}(x,y) + C_{1,2}(x,y) \times \tilde{E}_D^{(2)}(x,y) + C_{2,3}(x,y) \times \tilde{E}_D^{(3)}(x,y) \quad (6)$$

where $\tilde{E}_D^{(2)}$ and $\tilde{E}_D^{(3)}$ are resized to agree with the size of $E_D^{(1)}$ at scale level 1 from the normalized energies $E_D^{(2)}$ and $E_D^{(3)}$, respectively. The discriminant measure $S(x,y)$ is then resized to its full scale of $M \times N$. In this study, all of the resize operations are implemented with bilinear interpolation [48,49] to perform the wavelet decomposed subimage zooming.

Since a defect edge has a larger diagonal energy $E_D^{(\ell+1)}(x,y)$ and weight $C_{\ell,\ell+1}(x,y)$, the corresponding discriminant measure $S(x,y)$ of the defect edge can be significantly larger than that of a grain edge. Fig. 4 shows the effect of the weights before and after they are added to the discriminant measure in Eq. (6). Fig. 4(a) shows the solar wafer image containing a fingerprint defect in the lower-right corner of the image. Fig. 4(b) and (c) respectively present the discriminant measure $S(x,y)$ in a 3D perspective and as gray-value images, where larger values of potential defect points are presented with darker intensities. The smaller weights can suppress the normalized energy in defect-free regions, whereas the larger weights can enlarge the normalized energy in defect regions. The fingerprint defect region is clearly detected by the proposed discriminant feature $S(x,y)$. Fig. 4(d) shows the result of the unweighted model (i.e., setting all $C_{\ell,\ell+1} = 1$) in the proposed Eq. (6). The magnitude of the unweighted energy feature cannot significantly distinguish the defect regions from the normal crystal grain background. Fig. 4(e) shows the result of (d) as an intensity with an 8-bit display, where many noisy points are presented as defects. Therefore, the use of the average energy difference in two scale levels as weights can significantly improve the discriminant power for separating defects from the inhomogeneous texture background in the multicrystalline solar wafer image.

To segment the defect from the background in the $S(x,y)$ image, a simple thresholding process is used. If the discriminant measure $S(x,y)$ is significantly less than a threshold T_S , the pixel (x,y) in the original image is classified as a defect point. Otherwise, it is defect-free. The simple statistic process control (SPC) is applied to set up the threshold T_S for $S(x,y)$. The control limit (i.e., threshold) used to identify defect points is given by

$$T_S = \mu_S + K\sigma_S$$

where μ_S is the mean and σ_S is the standard deviation of measured values $S(x,y)$ for all pixels in the $M \times N$ image. Note that the threshold is adaptively calculated for each individual inspection image. The parameter K is a predetermined multiplication of the standard deviation from the mean. In the experiment, the control constant K is empirically given by 1.0 for all test images. A defect point will be set to 1 (shown in black) if the measured value is larger than the control limit, whereas a

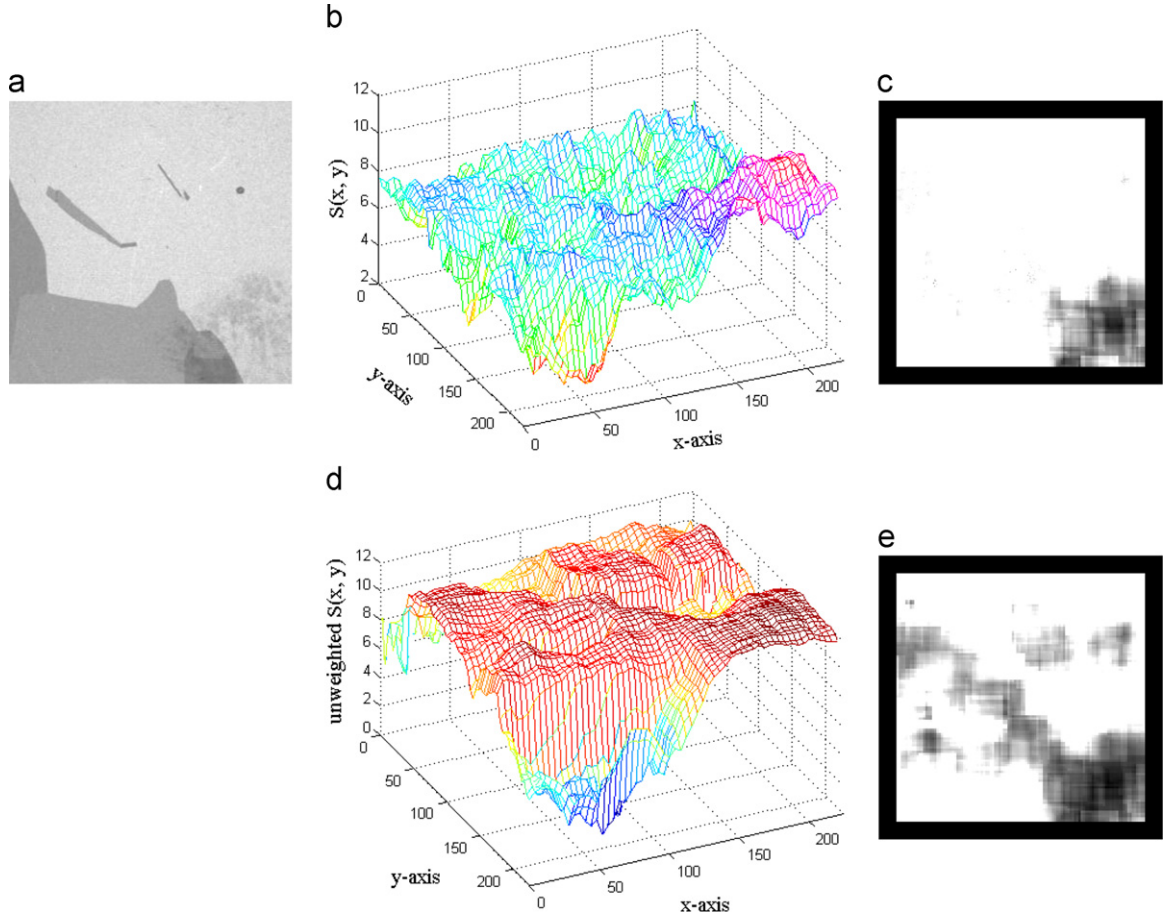


Fig. 4. (a) Fingerprint defect image; (b) 3D perspective of $S(x, y)$ with $C_{\ell, \ell+1}(x, y)$ as weights; (c) $S(x, y)$ values displayed as an intensity function of (b); (d) 3D perspective of $S(x, y)$ with $C_{\ell, \ell+1}(x, y) = 1$; (e) $S(x, y)$ values displayed as an intensity function of (d).

defect-free point will be set to 0 (shown in white) in the resulting binary image. The detection result then appears as a binary image $B(x, y)$. That is,

$$B(x, y) = \begin{cases} 1 \text{ (defective)} & \text{if } S(x, y) > \mu_S + K\sigma_S \\ 0 \text{ (defect-free)} & \text{otherwise} \end{cases}$$

2.2. Wavelet decomposition in gradient images

The crystal grains of a multicrystalline solar wafer show various gray-levels, which make the gray values of a defect indistinguishable in the multi-grain background. As a result, the local blurred defects are hard to distinguish from the similar gray-level background. The inhomogeneous background of a multicrystalline solar wafer surface can be simplified, and the defect can be further emphasized, to extract better discriminant features in the gradient image by applying the same wavelet decomposition process as described in subsection A. The Sobel operation is thus used to transform the original gray-level image of a solar wafer into a gradient image that shows a clearer distinction between defects and crystal grains.

The gradient image $G(x, y)$ of a wafer image $f(x, y)$ at pixel (x, y) is defined as

$$G(x, y) = \sqrt{G_x^2(x, y) + G_y^2(x, y)} \quad (7)$$

where

$$G_x(x, y) = \sum_{i=-1}^1 \sum_{j=-1}^1 f(x+i, y+j) a_x(i, j)$$

a			b		
-1	0	1	-1	-2	-1
-2	0	2	0	0	0
-1	0	1	1	2	1

Fig. 5. Sobel edge operators in (a) the x-axis ($a_x(i, j)$) and (b) the y-axis ($a_y(i, j)$).

$$G_y(x, y) = \sum_{i=-1}^1 \sum_{j=-1}^1 f(x+i, y+j) a_y(i, j)$$

where $a_x(i, j)$ and $a_y(i, j)$ are the Sobel edge operators in the x- and y-axes, respectively, and are given in Fig. 5. Fig. 6(a) shows the solar wafer surface with a saw-mark defect. The saw-mark defect displays blurred edges. It crosses over the whole image and separates the image into upper and lower parts with unclear edges. The grain boundary represents almost the same characters as the saw-mark defect in the gray-level image. Fig. 6(b) is the gradient image of (a), where the saw-mark edges are blurred and spread more widely and the grain edges are sharp and more concentrated. A small saw-mark defect region is marked by a square frame in the image, and the dotted-square frame indicates a regular grain region, as seen in Fig. 6(a). The box-plots in Fig. 6(c) and (d) measure individual discriminant measure $S(x, y)$ (see Eq. (6)) using the original gray-level image and the corresponding gradient image as the input image to

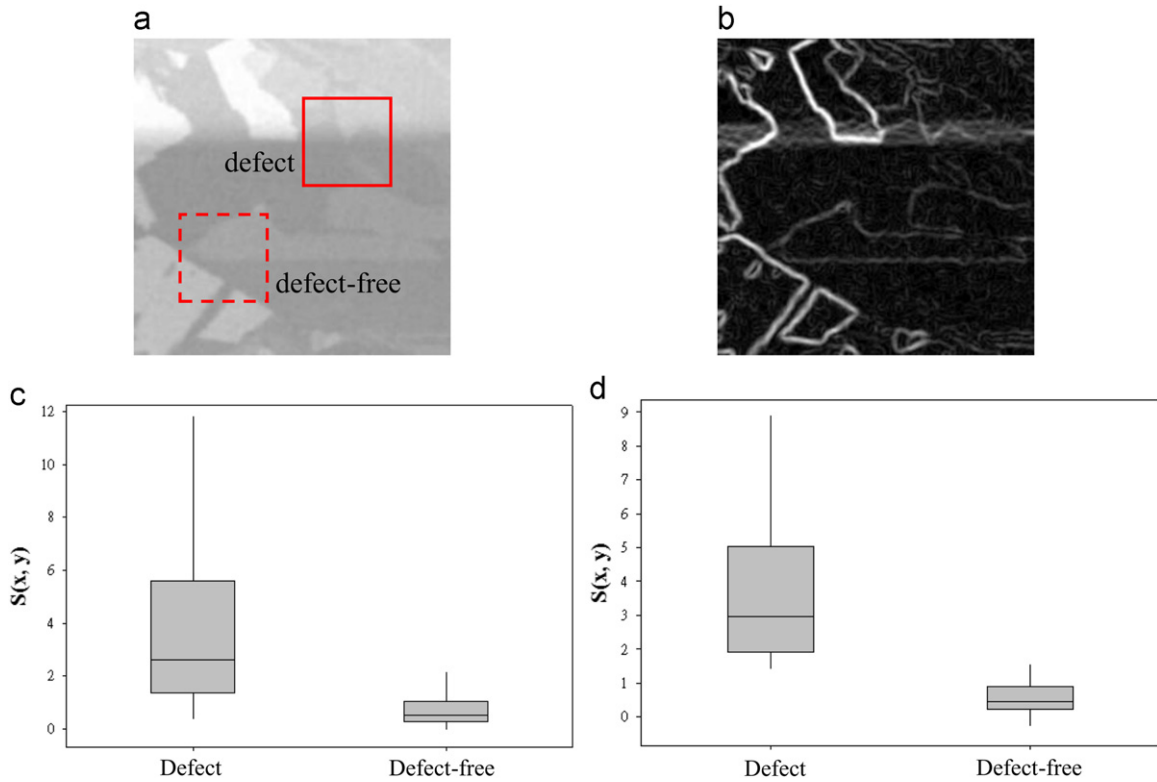


Fig. 6. (a) Solar wafer image containing a saw-mark defect; (b) gradient image of (a); (c) box-plot of $S(x,y)$ from the gray-level image (a) (Fisher ratio=0.217); (d) box-plot of $S(x,y)$ from the gradient image (b) (Fisher ratio=0.547).

the wavelet decomposition and feature extraction process. The box-plot in Fig. 6(c) shows that the saw-mark and regular grains in the gray-level image can be well distinguished. The discriminant measure obtained from the gradient image can further improve the detection capability, as shown in Fig. 6(d). The Fisher ratio [50] is calculated to indicate the separability of the detection results in gray-level and gradient images. A larger Fisher ratio of between-class variance and within-class variance gives a better discriminant power. The Fisher ratio of $S(x,y)$ in the gray-level image is 0.217, and the one in the gradient image is 0.547. In the subsequent experiments, defect detection in solar wafer surfaces is carried out by wavelet decomposition in gradient images.

3. Experimental results

The proposed algorithms were implemented on an Intel Core 2, 1.87 GHz CPU personal computer. The mean computation time of the proposed method was 0.23 s for a 256×256 image. The control constant K of the statistical control limit is set at 1 for defect detection. The neighborhood window size $w \times w$ is given by 9×9 . The parameter values of w and K are the same for all test samples in the experiments. The proposed defect detection scheme is applied to the gradient image of each test sample in the experiment. The effects of changes in parameter values of w and K are first presented in Section 3.1. The detection results of the test samples with various defect types are discussed in Section 3.2.

3.1. Effects of changes in window size and control constant

The proposed defect detection algorithms has only two main parameters: the window size $w \times w$ for the weight $C_{\ell,\ell+1}$ and the control constant K for the control limit. In order to evaluate the

effect of changes in the neighborhood window for the discriminant measure $S(x,y)$, Fig. 7 presents the detection results with varying window sizes of 5×5 , 9×9 , 13×13 and 17×17 , given that the control constant $K=1$. In the first column of the figure, the testing samples sequentially are two fingerprint defect images (a1)–(b1), two saw-mark defect images (c1)–(d1), and two defect-free images (e1)–(f1). A very small window size may misdetect subtle defects, whereas an excessively large window size may create random noise in defect-free images. As seen in Fig. 7(b2), the results show that the fingerprint defect is mis-detected when the neighborhood window size is only 5×5 . When the window size is too large, such as 17×17 , the noise is detected in the resulting binary image of defect-free solar wafers, as seen in Fig. 7(f5). In the third and fourth columns, fingerprint and saw-mark defects are well detected with window sizes of 9×9 and 13×13 . In consideration of computational efficiency and detection effectiveness, a window size of 9×9 was therefore selected in the subsequent experiments and is suggested for the system implementation.

The parameter K sets up the adaptive control limit (threshold) to segment the defect points from the background. A very small K value gives a tight control limit and may result in severe noise. Conversely, an excessively large K value yields a loose control limit and may fail to detect a subtle defect. Fig. 8 shows the detection results as binary images with varying control constants $K=0.5$, 1.0, 1.5 and 2.0, given the neighborhood window of size 9×9 . In the first column of the figure, the first four samples are defective images, wherein the first and second contain fingerprints and the third and fourth contain black line saw-marks. The last two samples are defect-free. They are exactly the same as the six test images in Fig. 7. When the control constant is tightly selected, such as $K=0.5$, the fingerprint (the first and second samples in (a1) and (b1)) can be well detected, and the stripe-type saw-mark (the third and fourth samples in (c1) and (d1)) can

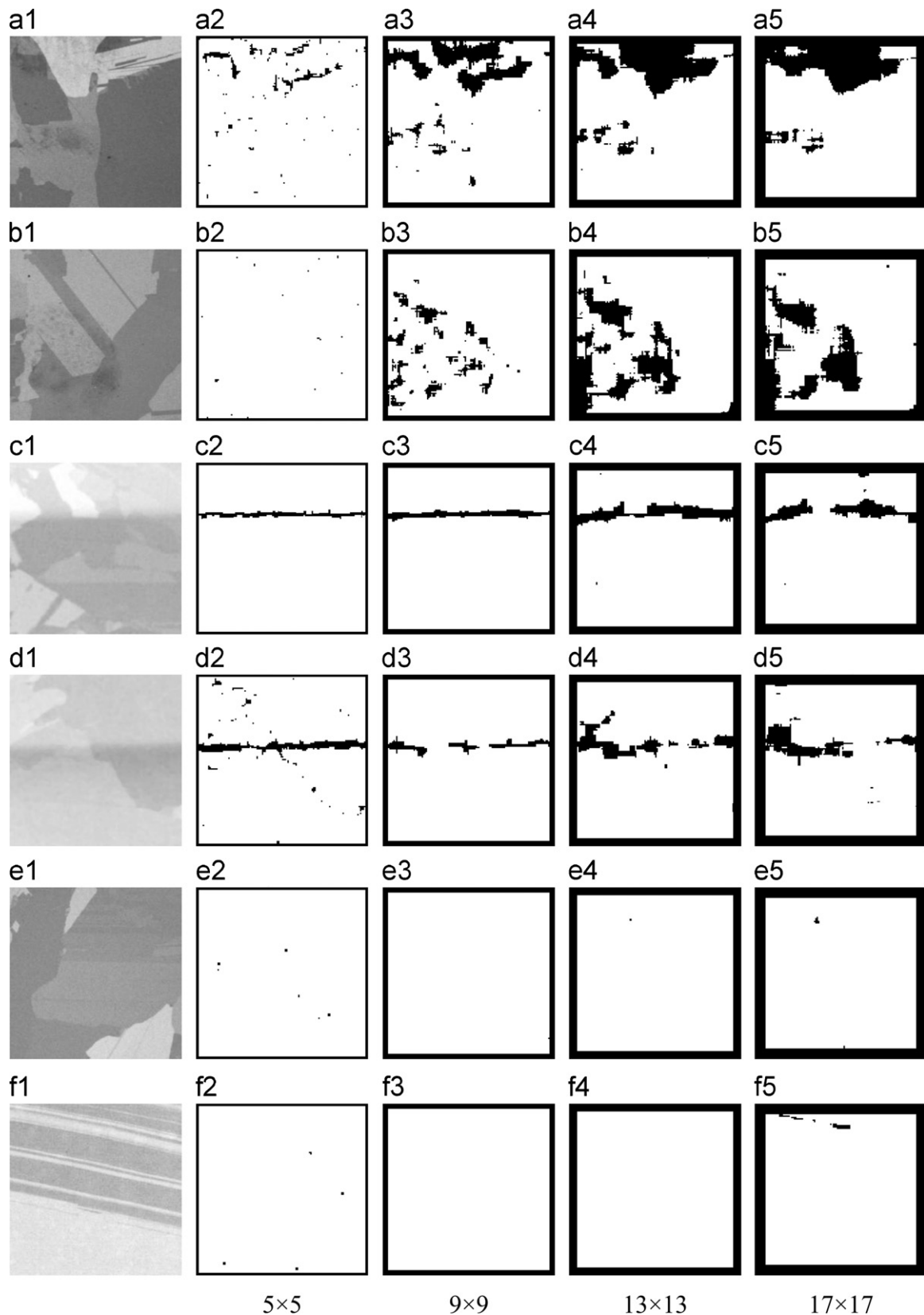


Fig. 7. Effect of changes in window size of 5×5 , 9×9 , 13×13 and 17×17 , given the control constant $K=1$: (a1), (b1) two fingerprint defect images; (c1), (d1) two saw-mark defect images; (e1), (f1) two faultless samples; (a2)–(f2) respective detection results of 5×5 ; (a3)–(f3) respective detection results of 9×9 ; (a4)–(f4) respective detection results of 13×13 ; (a5)–(f5) respective detection results of 17×17 .

also be well detected. However, there are some noisy points detected in the defect-free image, as seen in Fig. 8(f2). The random noise generated in the binary images of defect-free solar

wafers could be easily removed by simple morphological closing operations. Given a loose control limit, for example $K=2$, all the defect images are mis-detected. A control constant $K=1$ gives the

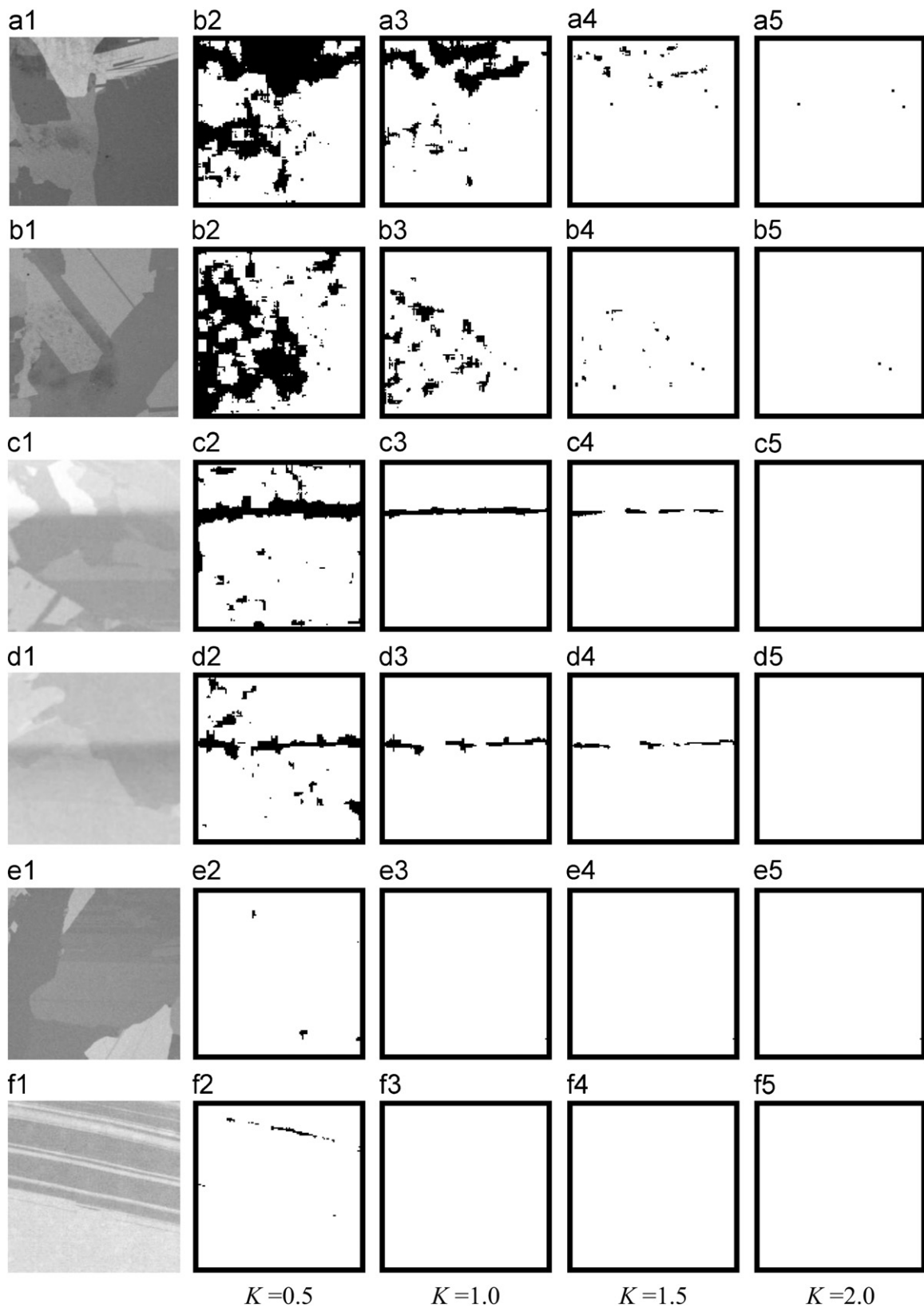


Fig. 8. Effect of changes in control constant with $K=0.5$, 1.0 , 1.5 and 2.0 , given the window size of 9×9 : (a1), (b1) two fingerprint defect images; (c1), (d1) two saw-mark defect images; (e1), (f1) two faultless samples; (a2)–(f2) respective detection results of $K=0.5$; (a3)–(f3) respective detection results of $K=1.0$; (a4)–(f4) respective detection results of $K=1.5$; (a5)–(f5) respective detection results of $K=2.0$;

best overall performance, where the random noise is removed and all the defects are well detected.

3.2. Solar wafer defect detection

Fig. 9 shows the detection results of the proposed method for defect-free images containing various grain patterns. Figs. 10–12

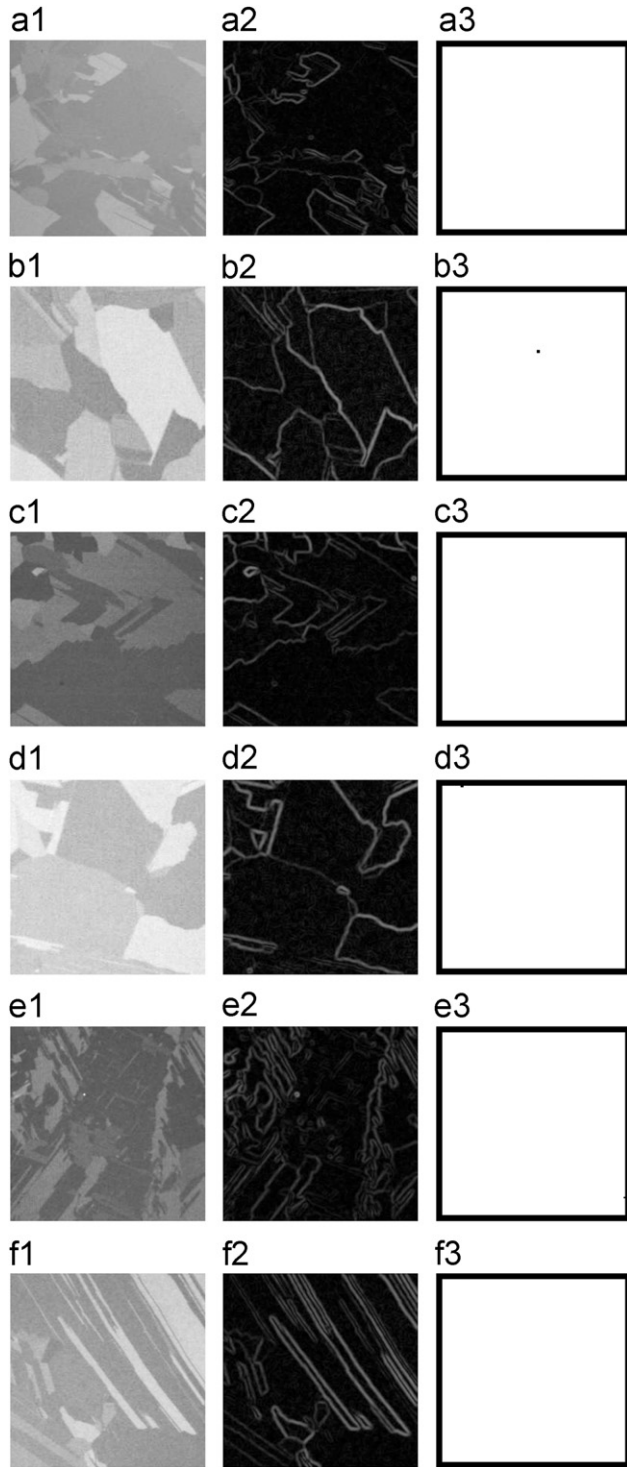


Fig. 9. Detection results of defect-free solar wafer images: (a1)–(f1) six faultless samples; (a2)–(f2) corresponding gradient images of (a1)–(f1); (a3)–(f3) respective detection results of the proposed inspection scheme, where no defects are declared.

show detection results of fingerprint, contaminant and saw-mark solar wafer images, respectively. In Fig. 9, the first column ((a1)–(f1)) presents six defect-free images for testing, and the second column ((a2)–(f2)) shows the corresponding gradient images of Fig. 9(a1)–(f1). The proposed defect detection method is implemented in these gradient images to get best results. The third column ((a3)–(f3)) presents the detection results of the proposed inspection scheme. Any suspected defect points are shown in black in the binary images. In this experiment, we used the morphological closing operation with a 3×3 structuring element to remove noise in the binary images. In the six defect-free test samples, each solar wafer image comprised a unique multi-grain pattern. The proposed defect-detection scheme can reliably ignore the grain edges in the detection process and results in clear surfaces in the final binary images with the same parameter setting.

Fig. 10(a1)–(e1) shows five defective solar wafer images containing fingerprint defects for testing. Fig. 10(a2)–(e2) illustrates the respective enhanced images of Fig. 10(a1)–(e1) by linearly stretching the original gray levels between 0 and 255 for 8-bit displays. The enhanced images, presented here only for better visualization of the subtle defects in the image, are not necessary in the proposed detection procedure. It can be seen from Fig. 10(b2) that the fingerprint defect is embedded between grain boundaries. It makes the inspection task extremely difficult. Fig. 10(a3)–(e3) are the respective gradient images of Fig. 10(a1)–(e1). Fig. 10(a4)–(e4) represent the detection results by superimposing the detected defect points in the binary image (colored black) on the original images, which accordingly present the detected positions and areas of detected defects. Fig. 11(a1)–(f1) shows further six contaminant defects on solar wafer images. Fig. 11(a2)–(f2) are respective enhanced images of Fig. 11(a1)–(f1) for better visualization of the defects. Fig. 11(a3)–(f3) illustrates the respective gradient images of Fig. 11(a1)–(f1). Fig. 11(a4)–(f4) indicates the detected defect areas of the proposed method. All of the tiny contaminants are well detected for either the dark contaminant (such as the test sample in Fig. 11(c1)) or the light one (such as the one in Fig. 11(a1)).

Fig. 12 presents six saw-mark defects in the solar wafer images for testing. Fig. 12(a1)–(c1) involve dark line saw-marks, which do not present clear saw-mark lines in the multi-grain background. The test samples in Fig. 12(d1)–(e1) present clear saw-mark lines in the images. Fig. 12(f1) contains a bright line saw-mark. Fig. 12(a1)–(e1) shows blurred saw-mark edges that divide the wafer surfaces into two regions, one (upper region) with brighter intensity and the other (lower region) with darker intensity. Fig. 12(f1) shows the saw-mark with a light line shape. All these complex saw-mark types hinder defect detection in the inhomogeneous grain background. Fig. 12(a2)–(f2) are the corresponding enhanced images of Fig. 12(a1)–(f1) for visualization. Fig. 12(a3)–(f3) displays the individual gradient images, where (a3)–(c3) do not present visible saw-mark edges in the gradient images. Fig. 12(a4)–(f4) shows the detected defect points in black on the original images. All of the saw-mark defects are well detected, regardless of the types of saw-mark.

In order to further verify the detection performance of the proposed method, a total of 96 solar wafer images were evaluated. Of these 96 images, 50 were defect-free and 46 were defective. All the parameter values were the same as those used in the previous experiment. The 46 defect images involved 25 saw-mark defect samples, 8 fingerprint defect samples, and 13 contaminant defect samples. The 25 saw-mark samples involved various saw-mark defects, including black lines, white lines, and white stripes. All of the detection statistics are summarized in Table 1. Forty-five of the 46 defective solar wafer images were correctly identified, and the false negative rate was 2% (1/46).

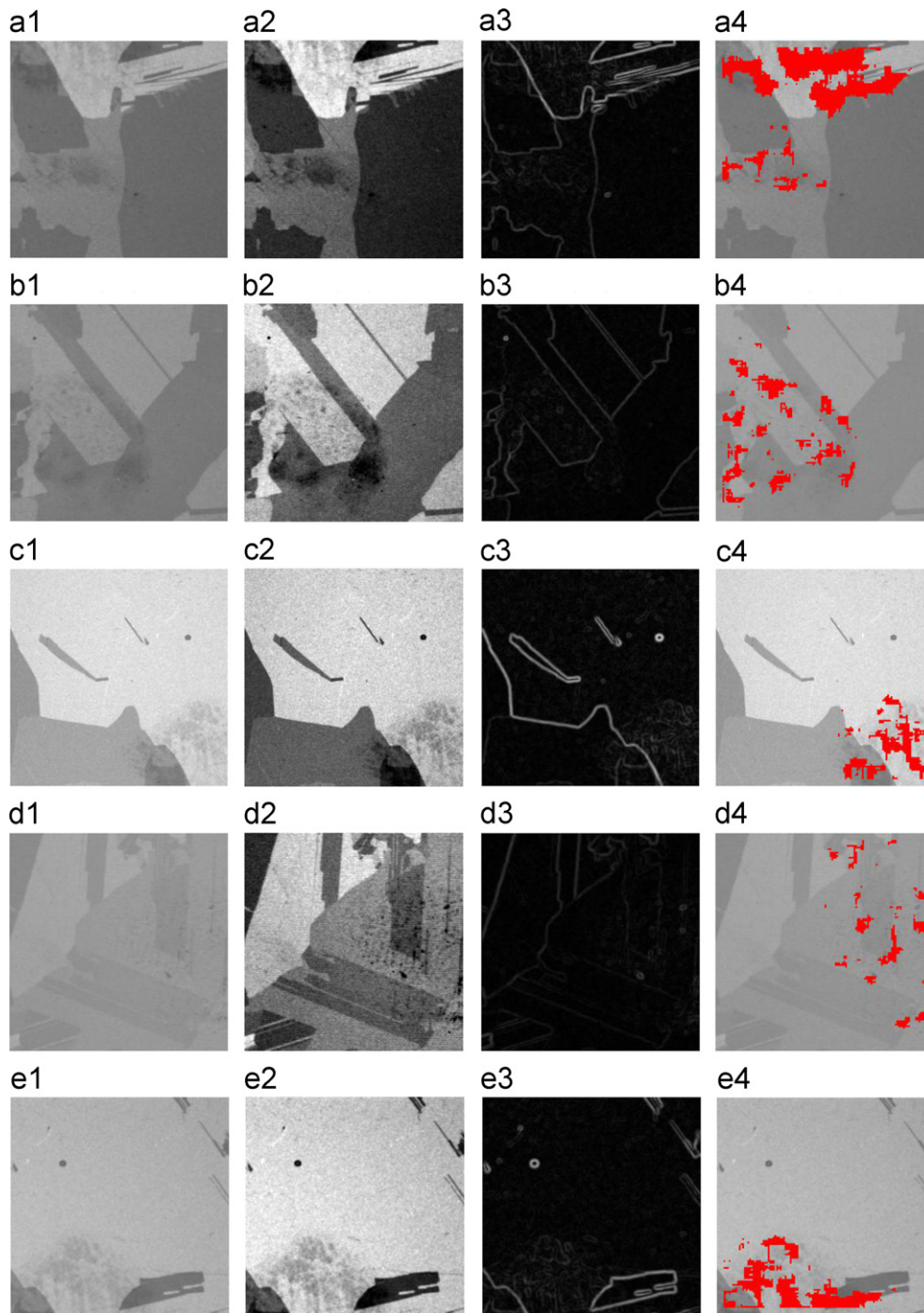


Fig. 10. Detection results of defective solar wafer images with fingerprint: (a1)–(e1) five fingerprint defect images; (a2)–(e2) respective enhanced images of (a1)–(e1) for better visualization of defects; (a3)–(e3) respective gradient images of (a1)–(e1); (a4)–(e4) detection results of the proposed inspection scheme by superimposing the detected defect points (shown in black) on the original images.

The mis-detected sample was a light-wear saw-mark. It is hardly observable in the image, as seen in Fig. 13(a). Fig. 13(b) is the enhanced image of Fig. 13(a). The wear saw-mark can now be better observed in the enhanced image, but it is still not clearly distinguishable from its surrounding background. Fig. 13(c) is the gradient image of Fig. 13(a), where no strong gradient magnitude can be visually observed along the horizontal edges of the saw-mark. Therefore, this sample was mis-detected in this study. No false alarms were generated for the 50 defect-free solar wafer images, and the false positive rate was zero for the test images in the experiment.

4. Conclusions

This paper has proposed a defect detection scheme based on wavelet decomposition techniques to identify various defects in multicrystalline solar wafers containing inhomogeneous grain patterns. The fingerprint, contaminant, and saw-mark defects, which show blurred edge characteristics with respect to sharp grain edges in the background, can be effectively separated by the proposed discriminant measure in wavelet-decomposed images. The discriminant measure is derived from the diagonal detail subimages in three wavelet-decomposed levels with a weighting

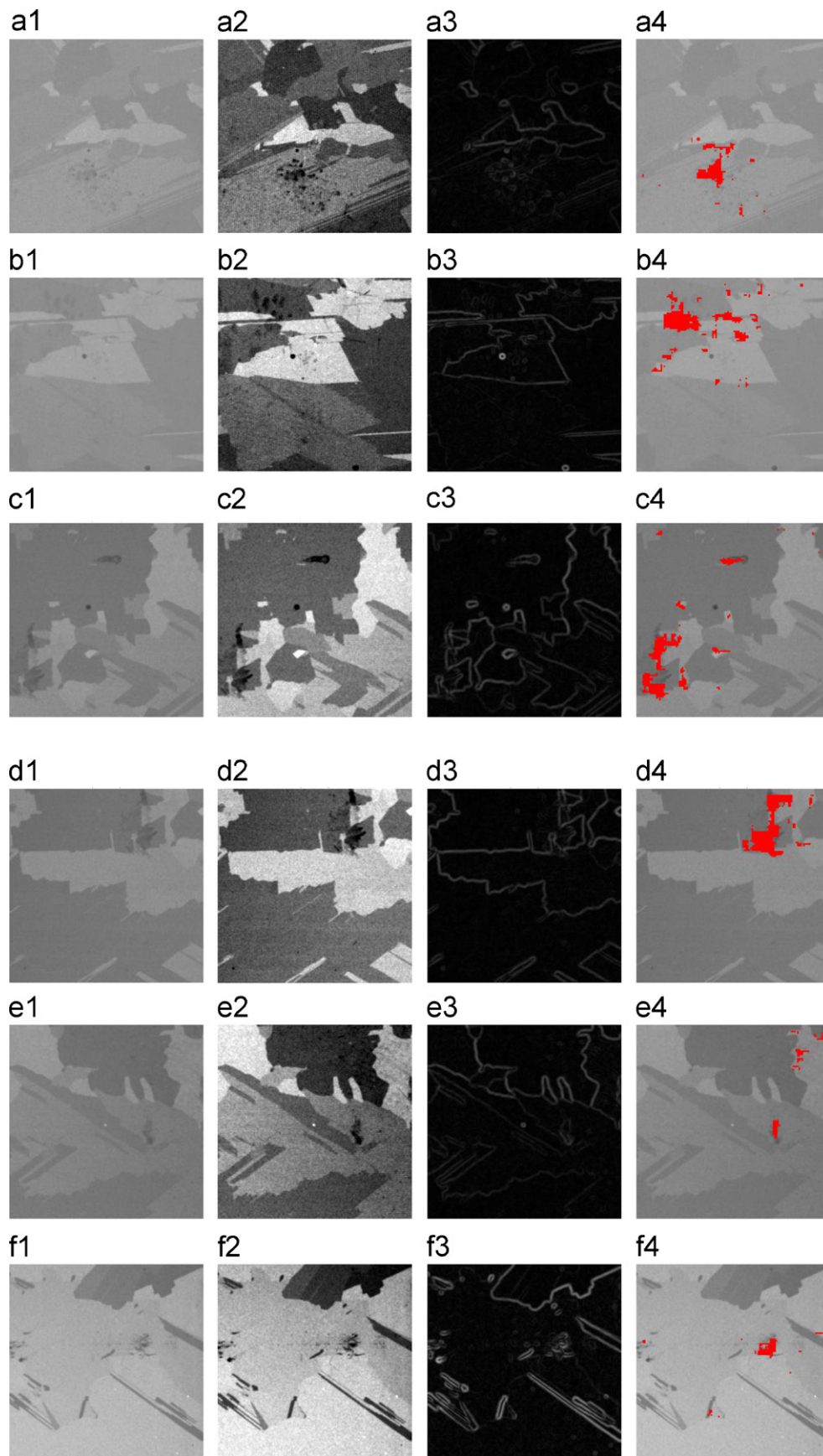


Fig. 11. Detection results of defective solar wafer images with contaminant: (a1)–(f1) six contaminant defect images; (a2)–(f2) respective enhanced images of (a1)–(f1); (a3)–(f3) respective gradient images of (a1)–(f1); (a4)–(f4) detection results of the proposed inspection scheme by superimposing the binary results (black pixels) on the original images.

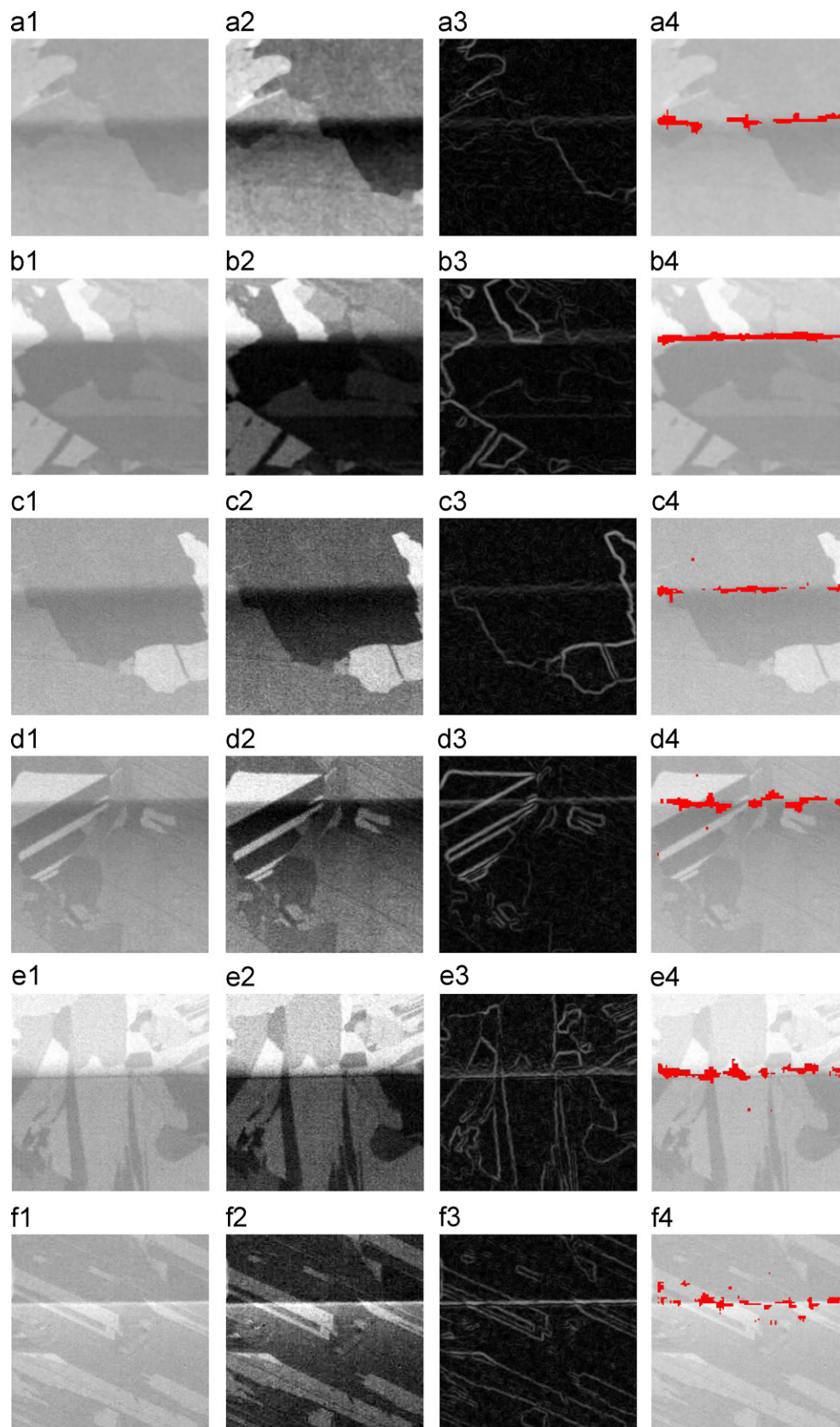
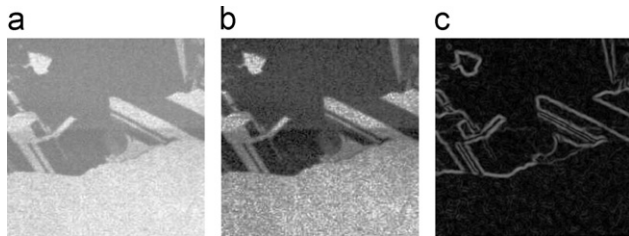


Fig. 12. Detection results of defective solar wafer images with saw-mark: (a1)–(f1) six saw-mark defect images; (a2)–(f2) respective enhanced images of (a1)–(f1); (a3)–(f3) respective gradient images of (a1)–(f1); (a4)–(f4) detection results of the proposed inspection scheme by superimposing the binary results on the original images.

Table 1

Detection results on the 98 test samples.

Sample types	Number of samples	Detection results	
		Defect	Defect-free
Defect-free	50	0	50
Defective			
Fingerprint	8	8	0
Contaminant	13	13	0
Saw-mark	25	24	1

**Fig. 13.** The mis-detected sample that contained a weak wear defect: (a) saw-mark image; (b) enhanced image of (a); (c) gradient image of (a).

factor based on the average energy difference between two consecutive scale levels.

The proposed method in its present form can be applied successfully to any defect types that involve relatively scattering and blurred edges on inhomogeneous solar wafer images. However, a severe micro-crack defect showing thin and sharp edges in the multicrystalline solar wafer cannot be effectively detected by the proposed method. It is believed that discriminant features for micro-crack inspection might exist in the wavelet decomposition. It is worthy of further investigation to find a generic inspection method for all types of solar wafer defects.

References

- [1] X. Xie, A review of recent advances in surface defect detection using texture analysis techniques, *Electronic Letters on Computer Vision and Image Analysis* 7 (2008) 1–22.
- [2] E.J. Yarmchuk, C.W. Cline, D.C. Bruen, Latent defect screening for high-reliability glass-ceramic multichip module copper interconnects, *IBM Journal of Research and Development* 49 (2005) 677–685.
- [3] S.M. Chao, D.M. Tsai, An anisotropic diffusion-based defect detection for low-contrast glass substrates, *Image and Vision Computing* 26 (2008) 187–200.
- [4] B. Tang, J.-Y. Kong, X.-D. Wang, G.-Z. Jiang, L. Chen, Steel strip surface defects detection based on mathematical morphology, *Journal of Iron and Steel Research* 22 (2010) 56–59.
- [5] M. Zhai, S. Fu, Applying target maneuver onset detection algorithms to defects detection in aluminum foil, *Signal Processing* 90 (2010) 2319–2326.
- [6] N.G. Shankar, N. Zhong, Z.W. Ravi, A real-time print-defect detection system for web offset printing, *Measurement: Journal of the International Measurement Confederation* 42 (2009) 645–652.
- [7] C.T. Su, T. Yang, C.M. Ke, A neural-network approach for semiconductor wafer post-sawing inspection, *IEEE Transactions on Semiconductor Manufacturing* 15 (2002) 260–266.
- [8] N.G. Shankara, Z.W. Zhongb, Defect detection on semiconductor wafer surfaces, *Microelectronic Engineering* 77 (2005) 337–346.
- [9] C.H. Yeh, F.C. Wu, W.L. Ji, C.Y. Huang, A wavelet-based approach in detecting visual defects on semiconductor wafer dies, *IEEE Transactions on Semiconductor Manufacturing* 23 (2010) 154–164.
- [10] C.S. Cho, B.M. Chung, M.J. Park, Development of real-time vision-based fabric inspection system, *IEEE Transactions on Industrial Electronics* 52 (2005) 1073–1079.
- [11] A. Kumar, Computer-vision-based fabric defect detection: a survey, *IEEE Transactions on Industrial Electronics* 55 (2008) 348–363.
- [12] D. Seiler, Dual exposure speeds solar cell inspection, *Photonics Spectra* 44 (2010) 238–248.
- [13] W.-J. Zhang, D. Li, Y. Feng, Investigation of visual inspection method for silicon solar cell, *Journal of Computer Applications* 30 (2010) 249–252.
- [14] A.R.A. Besari, R. Zamri, K.A.A. Rahman, M.D.M. Palil, A.S. Prabuwono, Surface defect characterization in polishing process using contour dispersion, in: *Proceedings of the International Conference of Soft Computing and Pattern Recognition*, 2009, pp. 707–710.
- [15] X. Li, S.K. Tso, S.P. Guan, Q. Huang, Improving automatic detection of defects in castings by applying wavelet technique, *IEEE Transactions on Industrial Electronics* 53 (2006) 1927–1934.
- [16] A.S. Tolba, H.A. Khan, A.M. Mutawa, S.M. Alsaleem, Decision fusion for visual inspection of textiles, *Textile Research Journal* 80 (2010) 2094–2106.
- [17] B.-H. Wang, H.-J. Wang, H.-N. Qi, Wood recognition based on grey-level co-occurrence matrix, in: *Proceedings of the International Conference on Computer Application and System Modeling*, 2010, V1-269–V1272.
- [18] C. Copot, S. Syafie, S. Vargas, R.D. Keyser, L.V. Langenhove, C. Lazar, Carpet wear classification based on support vector machine pattern recognition approach, in: *Proceedings of the International Conference on Intelligent Computer Communication and Processing*, 2009, pp. 161–164.
- [19] B. Dhanasekar, B. Ramamoorthy, Restoration of blurred images for surface roughness evaluation using machine vision, *Tribology International* 43 (2010) 268–276.
- [20] S.A.H. Ravanidi, N. Pan, The influence of gray-level co-occurrence matrix variables on the textural features of wrinkled fabric surfaces, *Journal of the Textile Institute* 102 (2011) 315–321.
- [21] A. Abdesslem, A multi-resolution texture image retrieval using fast Fourier transform, *Journal of Engineering Research* 7 (2010) 48–58.
- [22] F. Bianconi, A. Fernández, E. González, J. Armesto, Robust color texture features based on ranklets and discrete Fourier transform, *Journal of Electronic Imaging* 18 (2009) art. no. 043012.
- [23] M. Ralló, M.S. Millán, J. Escofet, Referenceless segmentation of flaws in woven fabrics, *Applied Optics* 46 (2007) 6688–6699.
- [24] Z. Su, Z. Wen, W. Qiao, S. Yi, X. Shi, Automatic identification of the fabric structure based on Fourier transform, *Journal of Information and Computational Science* 3 (2006) 527–534.
- [25] P. Bourgeat, F. Meriaudeau, K.W. Tobin, P. Gorria, Comparison of texture features for segmentation of patterned wafers, in: *Proceedings of the SPIE—The International Society for Optical Engineering*, 2004, pp. 179–190.
- [26] S.G. Mallat, A theory for multiresolution signal decomposition: the wavelet representation, *IEEE Transactions on Pattern Analysis and Machine Intelligence* 11 (1989) 674–693.
- [27] S.G. Mallat, Multifrequency channel decompositions of images and wavelet models, *IEEE Transactions on Acoustics Speech and Signal Processing* 37 (1989) 2091–2110.
- [28] I. Zavorin, J.L. Moigne, Use of multiresolution wavelet feature pyramids for automatic registration of multisensor imagery, *IEEE Transactions on Image Processing* 14 (2005) 770–782.
- [29] C.-H. Yeh, F.-C. Wu, W.-L. Ji, C.-Y. Huang, A wavelet-based approach in detecting visual defects on semiconductor wafer dies, *IEEE Transactions on Semiconductor Manufacturing* 23 (2010) 284–292.
- [30] M. Tabassian, R. Ghaderi, R. Ebrahimpour, Knitted fabric defect classification for uncertain labels based on Dempster–Shafer theory of evidence, *Expert Systems with Applications* 38 (2011) 5259–5267.
- [31] J. Scharcanski, Stochastic texture analysis for monitoring stochastic processes in industry, *Pattern Recognition Letter* 26 (2005) 1701–1709.
- [32] A. Serdaroglu, A. Ertuzun, A. Ercil, Defect detection in textile fabric images using wavelet transforms and independent component analysis, *Pattern Recognition and Image Analysis* 16 (2004) 61–64.
- [33] H.-D. Lin, C.-Y. Chung, W.-T. Lin, Principal component analysis based on wavelet characteristics applied to automated surface defect inspection, *WSEAS Transactions on Computer Research* 3 (2008) 193–202.
- [34] M. Ghazvini, S.A. Monadjemi, N. Movahhedinia, K. Jamshidi, Defect detection of tiles using 2D-wavelet transform and statistical features, *Wild Academy of Science, Engineering and Technology* 49 (2009) 901–904.
- [35] M.D. Yang, T.C. Su, N.F. Pan, P. Liu, Feature extraction of sewer pipe defects using wavelet transform and co-occurrence matrix, *International Journal of Wavelets, Multiresolution and Information Processing* 9 (2011) 211–225.
- [36] X.-W. Zhang, Y.-Q. Ding, Y.-Y. Lv, A.-Y. Shi, R.Y. Liang, A vision inspection system for the surface defects of strongly reflected metal based on multi-class SVM, *Expert System with Applications* 38 (2011) 5930–5939.
- [37] I. Ar, Y.S. Akgul, A generic system for the classification of marble tiles using Gabor filters, in: *Proceedings of the International Symposium on Computer and Information Sciences*, 2008, pp. 1–6.
- [38] X. Xie, M. Mirmehdi, Localising surface defects in random color textures using multiscale texem analysis in image eigenchannels, in: *Proceedings of the IEEE International Conference on Image Processing*, 2005, III-1124–7.
- [39] X. Xie, M. Mirmehdi, Texture exemplars for defect detection on random textures, in: *Proceedings of the International Conference on Advances in Pattern Recognition*, 2005, pp. 404–413.
- [40] X. Xie, M. Mirmehdi, TEXEMS: Texture exemplars for defect detection on random textured surfaces, *IEEE Transactions on Pattern Analysis and Machine Intelligence* 29 (2007) 1454–1464.
- [41] J.C. Liu, G. Pok, Texture edge detection by feature encoding and predictive model, in: *Proceedings of the International Conference on Acoustics, Speech, and Signal Processing*, 1999, pp. 1105–1108.
- [42] Z. Fu, Y. Zhao, Y. Liu, Q. Cao, M. Chen, J. Zhang, J. Lee, Solar cell crack inspection by image processing, in: *Proceedings of the International Conference on Business of Electronic Product Reliability and Liability*, 2004, pp. 77–80.

- [43] M.A. Ordaz, G.B. Lush, Machine vision for solar cell characterization, in: *Proceedings of SPIE*, 2000, pp. 238–248.
- [44] M. Pilla, F. Galmiche, X. Maldague, Thermographic inspection of cracked solar cells, in: *Proceedings of SPIE*, 2002, pp. 699–703.
- [45] D.M. Tsai, C.C. Chang, S.M. Chao, Micro-crack inspection in heterogeneously textured solar wafers using anisotropic diffusion, *Image and Vision Computing* 28 (2010) 491–501.
- [46] M. Antonini, M. Barlaud, P. Mathieu, I. Daubechies, Image coding using wavelet transform, *IEEE Transactions on Image Process* 1 (1992) 205–220.
- [47] D.M. Tsai, B. Hsiao, Automatic surface inspection using wavelet reconstruction, *Pattern Recognition* 34 (2001) 1285–1305.
- [48] R.C. Gonzalez, R.E. Woods, *Digital Image Processing*, Prentice-Hall, New Jersey, 2002.
- [49] K.T. Gribbon, D.G. Bailey, A novel approach to real-time bilinear interpolation, in: *Proceedings of Second IEEE International Workshop on Electronic Design, Test and Applications*, 2004, pp. 126–131.
- [50] A. Webb, *Statistical Pattern Recognition*, John Wiley & Sons, West Sussex, England, 2002.

Wei-Chen Li received the B.E. degree in Mechanical Engineering from the Chung-Hua University, Taiwan in 2004 and the M.S. degree in Mechanical and Aerospace Engineering from the Chung-Hua University in 2006. He is currently pursuing the Ph.D. in Industrial Engineering and Management at Yuan-Ze University. His research interests include automated visual inspection, object recognition and texture analysis.

Du-Ming Tsai received the B.S. degree in Industrial Engineering from the Tunghai University, Taiwan in 1981, and the M.S. and Ph.D. degrees in Industrial Engineering from Iowa State University, Ames, Iowa in 1984 and 1987, respectively. From 1988 to 1990, he was a Principal Engineer of Digital Equipment Corporation, Taiwan branch, where his work focused on process and automation research and development. Currently he is a Professor of Industrial Engineering and Management at the Yuan-Ze University, Taiwan. His research interests include automated visual inspection, object recognition and texture analysis.